Received: 10 February 2022 | Accepted: 2 August 2022

DOI: 10.1111/jopr.13590

ORIGINAL ARTICLE

ACP AMERICAN COLLEGE OF PROSTHODONTISTS Your smile. Our specialty.®

Biomechanical evaluation of customized root implants in alveolar bone: A comparative study with traditional implants and natural teeth

Qing Li DMD, PhD[1,2,4,5,#] | **Xinyue Zhang ME**[1,4,5,#] | **Chao Wang PhD**[3] | **Hongcheng Hu DMD, PhD**[2,4,5] | **Zhihui Tang DMD, MD**[2,4,5] | **Yubo Fan PhD**[3]

[1]Center of Digital Dentistry, Peking University School and Hospital of Stomatology, Beijing, China

[2]Second Clinical Division, Peking University School and Hospital of Stomatology, Beijing, China

[3]Key Laboratory of Biomechanics and Mechanobiology, Ministry of Education, Beijing Advanced Innovation Center for Biomedical Engineering, School of Biological Science and Medical Engineering, School of Engineering Medicine, Beihang University, Beijing, China

[4]National Center of Stomatology and National Clinical Research Center for Oral Diseases, Beijing, China

[5]National Engineering Research Center of Oral Biomaterials and Digital Medical Devices, Beijing, China

Correspondence
Dr. Chao Wang, School of Biological Science and Medical Engineering, Beihang University, 37 Xueyuan Road, Haidian District, Beijing 100191, PR China.
E-mail: 10896@buaa.edu.cn

Abstract

Purpose: To compare and evaluate density changes in alveolar bones and biomechanical responses including stress/strain distributions around customized root implants (CRIs), traditional implants, and natural teeth.

Materials and methods: A three-dimensional finite element model of the maxillary dentition defect, CRI models, traditional restored implant models, and natural teeth with periodontal tissue models were established. The chewing load of the central incisor, the traditional implant, and the CRI was 100N, and the load direction was inclined by 11° in the sagittal plane. According to the bone remodeling numerical algorithm, the bone mineral density and distribution were calculated and predicted. In addition, animal experiments were performed to verify the feasibility of the implant design. The results of the simulation calculations were compared with animal experimental data in vivo to verify their validity.

Results: No significant differences in bone mineral density and stress/strain distribution were found between the CRI and traditional implant models. The animal experimental results (X-ray images and histological staining) were consistent with the numerical simulated results.

Conclusions: CRIs were more similar to traditional implants than to natural teeth in terms of biomechanical and biological evaluation. Considering the convenience of clinical application, this biomechanical evaluation provides basic theoretical support for further applications of CRI.

KEYWORDS
Customized root implant, biomechanics, finite element analysis, bone density, anisotropy

Dental implants have been widely used since the 1960s, although preformed implants are becoming increasingly difficult to adapt to the individual conditions of patients with the development of noninvasive and precision medicine.[1–3] With novel manufacturing technology, customized root implants (CRIs) based on the anatomical features of teeth can be produced by electron beam melting (EBM).[4] The customized design of the implant and the abutment has reduced the complexity of the prosthetic steps required. From the perspective of clinical application, CRIs have simplified the implant procedure and evidence suggests that CRIs improve the preservation of hard and soft tissue surrounding the implant.[5,6]

In clinical practice, the CRI adapts well to the soft and hard tissues of the patient because it is based on the anatomy of a natural root.[3] Mangano et al investigated the clinical effect of 15 CRIs prepared by direct laser metal sintering and found that there was no loosening or infection in any of the implants at the 1-year follow-up.[7] Liu et al confirmed the effect of porous microstructures on osseointegration of customized root dental implants through animal experiments.[8] Moin et al evaluated the feasibility of a commercially available immediate root analog implant system Replicate (Natural Dental Implants).[9] However, the distribution of stress and strain around CRIs and bone density changes compared to natural

[#]Qing Li and Xinyue Zhang contributed equally to the present study, and Xinyue Zhang should be regarded as co-first author.

teeth and traditional dental implants remain unclear. In order to determine the distribution of stress/strain around CRIs, the simulation was performed to evaluate the biomechanics of CRIs compared to the natural teeth and traditional dental implants, and to analyze bone remodeling induced by dental implants in this study.

Therefore, the purpose of this study was to compare and evaluate the changes in alveolar bone density and biomechanical response around CRIs, traditional implants, and natural teeth. Based on the bone "mechanostat" theory, simulation analysis has been carried out to investigate the variation in bone density distribution induced by dental implants.[10–12] As this is a novel implant, long-term clinical application data is not available. Simulation analysis can be used as supporting data to understand the adaptive changes of bone tissue around CRIs. Subsequently, the effectiveness of the finite element models and the feasibility of implant design were validated by animal experiments in vivo.

MATERIALS AND METHODS

Establishment of the finite element model

Based on the clinical CT images of the adult male maxilla, the geometric characteristics of the maxilla were extracted, and a 3D finite element model of the maxillary dentition defect was established. The CT image consisted of 421 transected sections with 0.625 mm spacing and a pixel width of 0.398 mm. Geometric models were built using the 3D image processing software Mimics (Materialize, Leuven, Belgium) and the reverse engineering software Geomagic Studio (Geomagic Company, NC). The portion of cancellous bone is set to be low-density bone tissue, while surrounding cancellous bone is cortical bone with an average thickness of 2 mm. (Fig 1d). The maxillary model consisted of cortical bone, cancellous bone, maxillary dentition, and periodontal membrane. In order to facilitate the simulation analysis, a partial region with a thickness of 15mm was selected from the maxillary model at the position of the central incisor as the local model.

Based on the 3D maxillary local model, CRIs, traditional restored implants, and natural teeth with periodontal tissues were placed in the maxillary right central incisor area. CRI models, traditional restored implant models, and natural teeth with periodontal tissue models were established (Fig 1A-C). The CRI was a one-piece design made of titanium alloy (Ti6Al4V), the traditional implant and abutment were made of pure titanium (Grade IV), and the crown was made of metal-fused porcelain restoration material. The implant geometry model was created using the CAD design software Solidworks, as shown in Figure 1E (SolidWorks Corp, Dassault Systemes Concord, MA); the average thickness of the native periodontal ligament (PDL) was 0.2 mm.

This model was meshed with the finite element software ANSYS Workbench (Swanson Analysis System Co., Houston, TX) using a 10-node tetrahedral element. To ensure the balance between the calculation accuracy and calculation efficiency of the model, a convergence test was performed. The overall model was meshed with an element size of approximately 0.5 mm, while local fine structures such as periodontal ligaments and implants were meshed with an element size of 0.05 mm. Finally, the Model A natural tooth model contained 62,805 elements, Model B traditional implant model contained 63,573 elements, and Model C included 53,721 elements. The detailed element assignments and node data are shown in Table 1. The specific finite element models are shown in Figure 1A-C, including dental implants, crowns, natural teeth, periodontal ligament, cortical bone, and cancellous bone.

The amount of chewing load in the simulation was set to the same value for convenience of comparison. The load of the central incisor, the traditional implant, and the CRI was 100N, and the load direction was inclined by 11° in the sagittal plane (Fig 1A-C).[15] The interface between the implant and bone tissue was set to simulate an osseointegration state. As displacement boundary conditions, the upper, distal, and near mid-planes of the maxilla were completely fixed to limit their movement.

The mechanical properties of the teeth, periodontal ligament, and implant system were set as linear elastic, homogeneous, and isotropic materials, as listed in Table 2. The initial state of the maxillary bone tissue is a homogeneous orthotropic material, and its material properties change with the adjustment of bone remodeling. For cortical bone and cancellous bone, the initial material properties are listed in Table 3.[16,17]

In Table 3, E_1, E_2, and E_3 are the elastic moduli in directions 1, 2, and 3, respectively; G_{12}, G_{13}, and G_{23} are the corresponding shear moduli; and v_{12}, v_{13}, and v_{23} are the corresponding Poisson's ratios. E_1 is in the mesiodistal direction, E_2 is in the buccal-lingual direction, and E_3 is in the direction of the mandible and maxilla. The initial densities of cancellous and cortical bones were set to 0.80 and 1.74 g/cm^3, respectively.

It should be noted that the cancellous bone and the cortical bone in this simulation follow different bone remodeling control equations. According to the relationship between bone density ρ (g/cm^3) and the elastic modulus Ei (MPa) in the following formula, the material properties of different bone tissues change according to the bone remodeling process.

Control equation for cortical bone remodeling[18]

$$\begin{cases} E_1 = 6382 + 255 \times (41965\rho) \\ E_2 = -13050 + 13000\rho \\ E_3 = -23930 + 24000\rho \end{cases} \quad \left(1.2 \le \rho_{\text{cortical}} \le 2.0\ \text{g/cm}^3\right) \tag{1}$$

Control equation for cancellous bone remodeling:[19]

$$\begin{cases} E_1 = 2349\rho^{2.15} \\ E_2 = 1274\rho^{2.12} \\ E_3 = 194\rho \end{cases} \quad \left(0.6 \le \rho_{\text{trabecular}} \le 1.2\ \text{g/cm}^3\right) \tag{2}$$

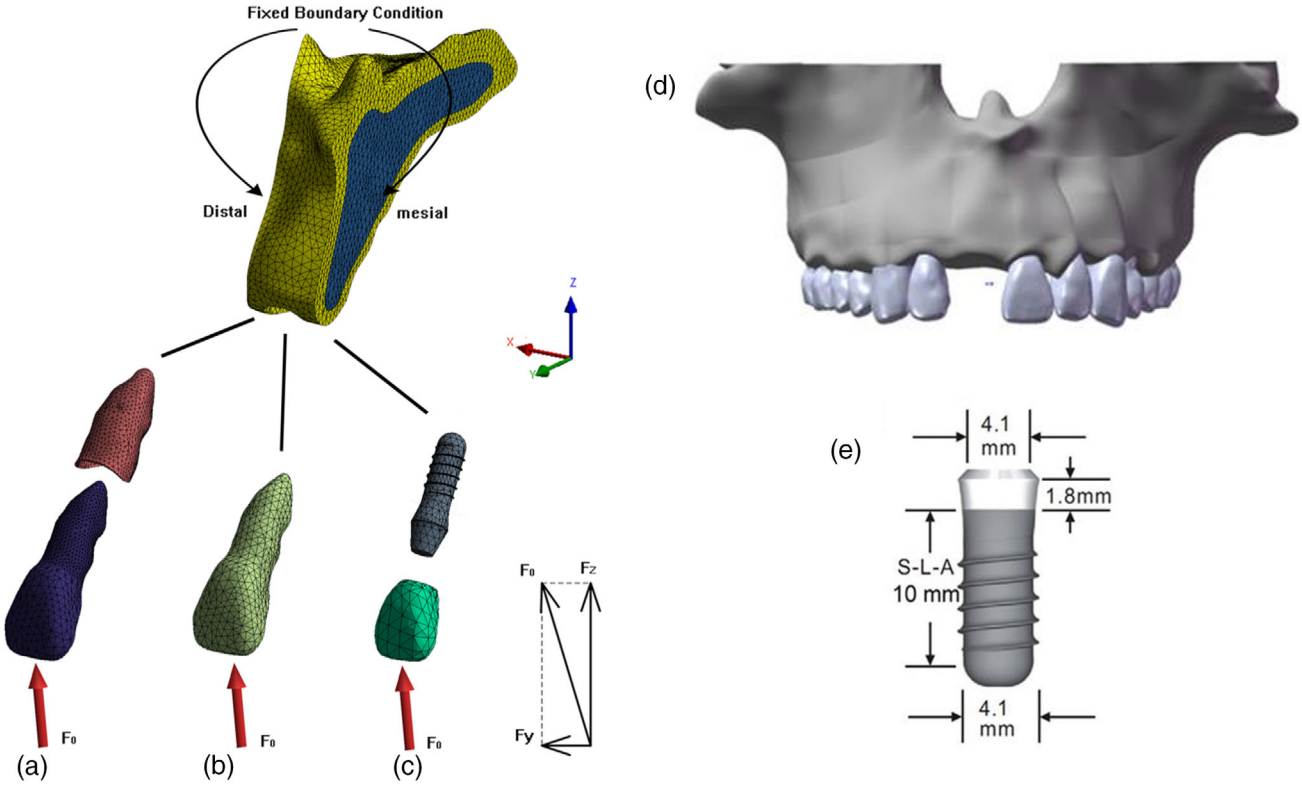

FIGURE 1 Three-dimensional finite element model of maxillary dentition and implant. (a) Natural central incisors with periodontal ligament. (b) Customized Root Implant, CRI. (c) Traditional implant with abutment and crown restored model. (d) Three-dimensional finite element model of maxillary dentition defect. (e) Straumann® soft tissue level aesthetic implant system was used in this study. The length of cylindrical implant was 10 mm, the diameter was 4.1 mm (conventional neck design, Φ 4.1 mm, RN), the neck height was 1.8 mm, Morse taper was 8°, and the implant abutments were connected with internal octagon.

TABLE 1 Number of elements and nodes in the finite element model

	(A) Natural tooth		(B) CRI		(C) Traditional implant	
Body name	**Elements**	**Nodes**	**Elements**	**Nodes**	**Elements**	**Nodes**
Cortical bone	16246	27888	16022	15034	15363	25751
Trabecular bone	24974	38106	24852	38002	37352	55769
Teeth	3290	6118				
PDL	18295	37134				
Dental implants			10035	16852	8131	14430
Crowns			2812	5132	2727	4950

CRI, customized root implant; PDL, periodontal ligament.

TABLE 2 Material properties of the tooth, periodontal ligament, and implant system in the finite element model[13,14]

Material	**Density (g/cm^3)**	**Elastic modulus (MPa)**	**Poisson's ratio**
Dentine	1.20	18600	0.31
PDL	0.70	70.3	0.45
Titanium alloy implant	4.51	110000	0.35
All-ceramic crowns	5.68	190000	0.28
Cortical bone	1.20-2.00	Equation (1)	0.31
Cancellous bone	0.60-1.20	Equation (2)	0.30

PDL, periodontal ligament.

TABLE 3 The initial material properties of the cortical bone and cancellous bone in the bone remodeling simulation[16,17]

	E_1 (GPa)	E_2 (GPa)	E_3 (GPa)	v_{12}/v_{21}	v_{23}/v_{32}	v_{31}/v_{13}	G_{12} (GPa)	G_{23} (GPa)	G_{31} (GPa)
Cortical bone	10.8	13.3	19.4	0.309/0.381	0.224/0.328	0.445/0.249	3.81	4.63	4.12
Cancellous bone	3	1	0.2	0.3	0.3	0.3	1.15	0.38	0.077

E_1, E_2, and E_3 are the elastic moduli directions; G_{12}, G_{13}, and G_{23} are the corresponding shear moduli; and v_{12}, v_{13}, and v_{23} are the corresponding Poisson's ratios.

As shown in Table 1, the dental implants and crown dentures in the finite element calculations were set to linear homogeneous material properties. In the calculation of bone remodeling, the elastic modulus of cancellous and cortical bones changes according to the relationship between the apparent density and elastic modulus (Equations (1) and (2)).

Orthotropic anisotropy bone remodeling algorithm

In this study, the strain energy density was used as the bone remodeling excitation value. The amount of local bone density change depends on the mechanical excitation Ψ (strain energy density per element mass), and the specific mathematical description equation is shown in Equations (3) to (6).

Bone resorption:

$$\Delta\rho = B\left(\Psi - (1-\delta)K_{ref}\right)\cdot\Delta t \qquad \text{if } \Psi < (1-\delta)K_{ref} \quad (3)$$

Bone equilibrium:

$$\Delta\rho = 0 \qquad \text{if } (1-\delta)K_{ref} \le \Psi \le (1+\delta)K_{ref} \quad (4)$$

Bone formation:

$$\Delta\rho = B\left(\Psi - (1+\delta)K_{ref}\right)\cdot\Delta t \qquad \text{if } (1+\delta)K_{ref} < \Psi \quad (5)$$

Bone overload resorption:

$$\Delta\rho = B\left(K_{overloading} - \Psi\right)\cdot\Delta t \qquad \text{if } \Psi \ge K_{overloading} \quad (6)$$

Here, the constants during bone remodeling were set to: B = 1.00 $(g/cm^3)^2$/(MPa time elements), K_{ref} = 0.004 J/g and δ = 10%, where B is the bone remodeling rate constant, K_{ref} is the bone remodeling physiological critical threshold and the overload absorption threshold, and δ is the width of the inert region, as previously described. [14,20,21]

Equations (3) to (6) were rewritten into Equations (7) to (9) using the Adams-Bashforth numerical algorithm. In the numerical calculation, the calculated value of the t_{n+1} iterations was calculated using the results of the t_{n-1} and t_n times:

$$\rho_1 = \rho_0 + \Delta t\, f(0) \quad (7)$$

$$\rho_{n+1} = \rho_n + \Delta t\left(\frac{3}{2}f_n + \frac{1}{2}f_{n-1}\right) \quad (8)$$

$$e = \frac{|\rho_{n+1} - \rho_n|}{\rho_n} \times 100 \quad (9)$$

Here, Δt is the time step increment, f_n is the amount of change in bone density, and e is the rate of change in bone density.

According to the above equation, the amount of change in local bone density was calculated at each time step, and then the corresponding local elastic modulus was updated according to Equations (1) and (2). Based on the updated material properties, a new round of finite element calculations and bone remodeling simulations was performed until the convergence criterion was reached. The convergence criterion: when the bone mineral density variation range in the simulation is within 3%, the calculation is considered to have converged. The FE-based bone remodeling calculation was coded using the APDL programming facility in the ANSYS software package. The entire bone remodeling process can be predicted mathematically and is summarized in a simplified flow chart in Figure 2.

In this simulation, the bone density converged after approximately 500 iteration cycles. Due to the use of iterative computing technology, the concept of time in the simulation actually represents the number of iterations, and each iteration can be considered to represent a period of time. In this study, 500 iteration cycles correspond to an initial remodeling cycle for human bones.

ANIMAL EXPERIMENT

Experimental animals

Three healthy adult male Beagle dogs (weight, 11.5 kg; age 1.5 years; Weitong Lihua Co., Ltd., animal license number: SCXK Beijing 2011-0003) were used in this study.

The left upper incisor was selected as the experimental tooth position. The inclusion criteria included sufficient bone height and bone width around the upper anterior teeth, and the adjacent teeth on both sides were suitable to fix the implant. Exclusion criteria included poor oral hygiene and acute periodontal infection. Each Beagle dog was kept in a separate cage with regular daily feeding. The study was approved by the Institutional Review Board (IRB) of the Ethical Committee of Peking University (LA2012-63).

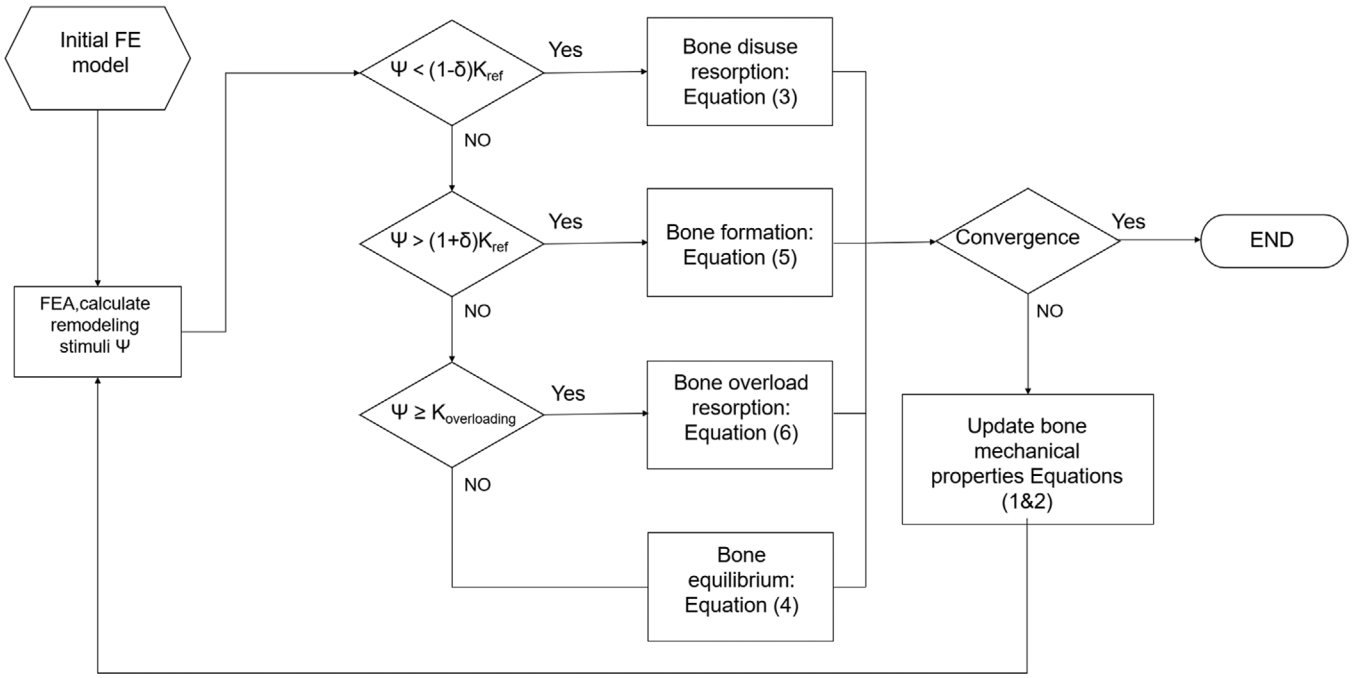

FIGURE 2 Schematic representation of the iterative flow chart for bone remodeling simulation.

Design and manufacture of CRIs

The oral soft and hard tissues of the Beagle dogs were thoroughly examined before the surgery and scanned using a computed tomography NewTom VG CBCT (Aperio Services, Italy) with 150 μm voxel. The CBCT data was converted into DICOM format and transferred into Mimics Design Software 10.01 (Materialise, USA) to reverse the three-dimensional reconstruction structure of the maxilla. A three-dimensional model of the left maxillary second incisor was extracted and saved in STL format (Fig 3A). In the process of data extraction by software, the width and thickness of the alveolar crest, density of the cortical plate and cancellous bone, and contour of the tooth were accurately evaluated for each tooth position.

According to the above digital data, the CRI was designed by a dentist and then produced by EBM technology. The Ti6Al4V alloy (AP&C, Canada) was melted using an EBM machine (Arcam EBM Q10, Sweden) using an electron beam as the energy source for manufacturing (particle size of powdered alloy: 45 to 100 μm; vacuum degree: $< 1 \times 10^{-4}$ mbar; maximum forming volume: 200 × 200 × 180 mm; electron beam power: 50 to 3000 watts; electron beam scanning speed: up to 8000 m/s; electron beam size: 0.2 mm). The surface of the implant directly produced by the EBM machine exhibited a rough surface structure with a Ra value of 66.8, an Rq value of 77.55, and an Rz value of 358.3 μm (Fig 3B). To clean the residual particles generated during the production process, the sample was sonicated in deionized water for 5 minutes, plasma-cleaned for 120 seconds, and placed in 0.9% physiological saline for storage. The CRI was designed as a crown-integrated, crown-polished, root-maintaining rough surface, and the root and neck were reduced by 0.1 to 0.3 mm in the range of 2 mm (Fig 3C).

Minimally invasive extraction and immediate implantation

The Beagle dogs were anesthetized with 2% sodium pentobarbital hydrochloride (30 mg/kg). Probing depth (PD), bleeding on probing (BOP), and clinical mobility of the teeth were examined. Digital periapical radiography was performed on the left upper incisor (Fig 4A).

The left upper incisor was extracted using a minimally invasive extraction device (Fig 5A). The extraction socket was rinsed with saline (0.9% NaCl), and periapical radiography was performed (Fig 4B). The CRI was implanted (Fig 5B), clinical mobility was measured, and the periapical radiograph was taken immediately and 3 months after the procedure (Fig 4C and D). CBCT images were collected. A strong fiber and a flow resin were used to adhere the crown of the CRI to the adjacent teeth crowns to increase implant stability and promote postoperative healing (Fig 5C).

Postoperative care

On the day of surgery and 5 days after surgery, 40,000 U/kg of penicillin was intramuscularly injected, and a fluid-restricted diet was commenced. Chlorhexidine acetate gargle (0.12 %) was applied regularly to scrub the CRI around the crown for 7 days.

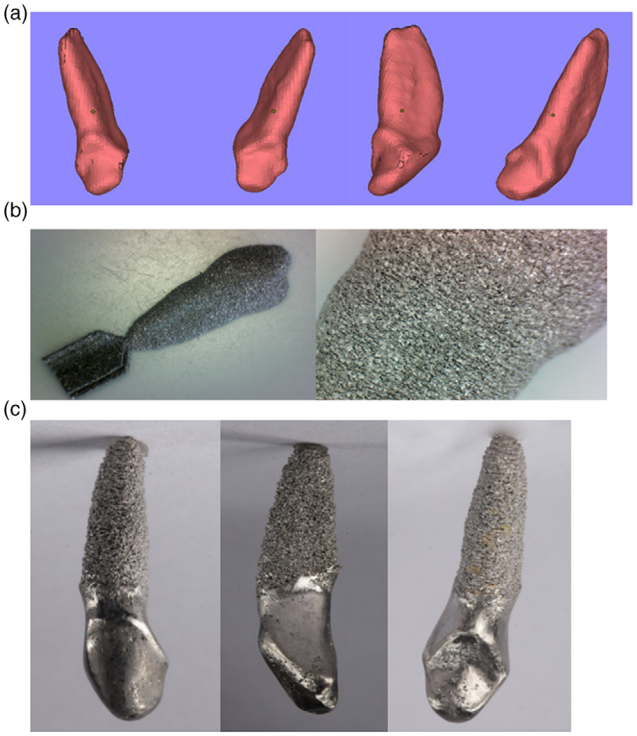

FIGURE 3 (a) Customized Root Implant STL format. (b) The surface of the implant produced by EBM shows a rough surface structure. (c) The Customized Root Implant was designed as a crown-integrated, crown-polished height; the roots maintain the original rough surface, and the root and neck were reduced by 0.1 to 0.3 mm in the range of 2 mm.

Specimen processing

Assessment of clinical indicators such as PD, BOP, and mobility of teeth, was conducted and 3 months after the procedure, digital periapical radiography was performed. Intravenous injection of 10% formalin fixative was used for execution and pre-fixation. The specimens were treated with 10% formalin solution (Fig 5D).

Specimens were scanned using micro-CT (SIEMENS, Germany) and 3D reconstructed (scanning voxel 26.2 μm, reconstruction layer thickness 52 μm). The plastic embedding technique was used to obtain soft and hard tissue implants, and a Leica 1600 hard tissue microtome was used to cut the embedded specimen of the implant with both soft and hard tissues of 200-μm thickness. Histological changes in the soft and hard tissues of the implants were observed after toluidine blue staining.

RESULTS

Qualitative comparison of bone density distribution

To clearly demonstrate the simulation results of the apparent density distribution of the bone, two observation sections of the sagittal plane (left) and coronal plane (right), are shown in Figure 6A. The results of the alveolar bone were specifically shown to concisely illustrate the effect of different implants/roots on the surrounding bone. The different colors in the figure legend represent a density distribution from 0.4 to 2.0 g/cm^3. The density distributions of the three models of natural teeth, CRI, and traditional implants are shown in Figure 6A. The density distribution patterns of the two implant models presented some similarities, and the high-density areas (1.68 to 2.00 g/cm^3) were concentrated in the cervical cortical bone region around the osseointegrated implant.

The difference between the CRI and the traditional implant was that high-density bone tissue appeared around the presence of threads. The distribution of the density region of the natural tooth was different from that of the two implant models. In the two implant models, bone formation was mainly concentrated in the cervical region, while in the natural tooth model, bone formation was uniformly generated around the natural root. It was observed that the implant model, whether root implants or cylindrical implants, had a different bone density distribution than the natural tooth model. High-density areas appeared evenly around the natural tooth model due to the PDL. The density distributions of the two implant models were similar, and increased density in the cervical regions around the implants was observed.

Quantitative comparison of bone density values

The bone mineral densities of the three models are quantitatively shown in Figure 6C. The abscissa represents the bone density values in g/cm^3, and the ordinate represents the percentage of bone mineral density values in the model. The distribution range of 0.6 to 1.2 g/cm^3 represents the cancellous bone area of the alveolar bone, it can be seen that the density distribution of the CRI and the traditional implant is similar, mainly concentrated in the range of 0.6 to 0.8 g/cm^3. The distribution of density is evenly distributed from 0.4 to 1.2 g/cm^3 among the implant models. The cortical bone was in the range of 1.6 to 2.0 g/cm^3. It can be seen that the densities of the three models are very similar in this region. Overall, the bone around the natural teeth tended to have a relatively dispersed distribution, while the bone density around the implants was more concentrated.

EVALUATION OF CRI BIOLOGICAL PROPERTIES IN VIVO

Clinical examination

The PD of the maxillary anterior teeth before extraction was 1 to 2 mm, and there was no obvious redness or swelling of the gums. There was no BOP or clinical mobility of the teeth. The left upper incisor was minimally invasive and completely extracted, and no root fracture, alveolar bone fracture,

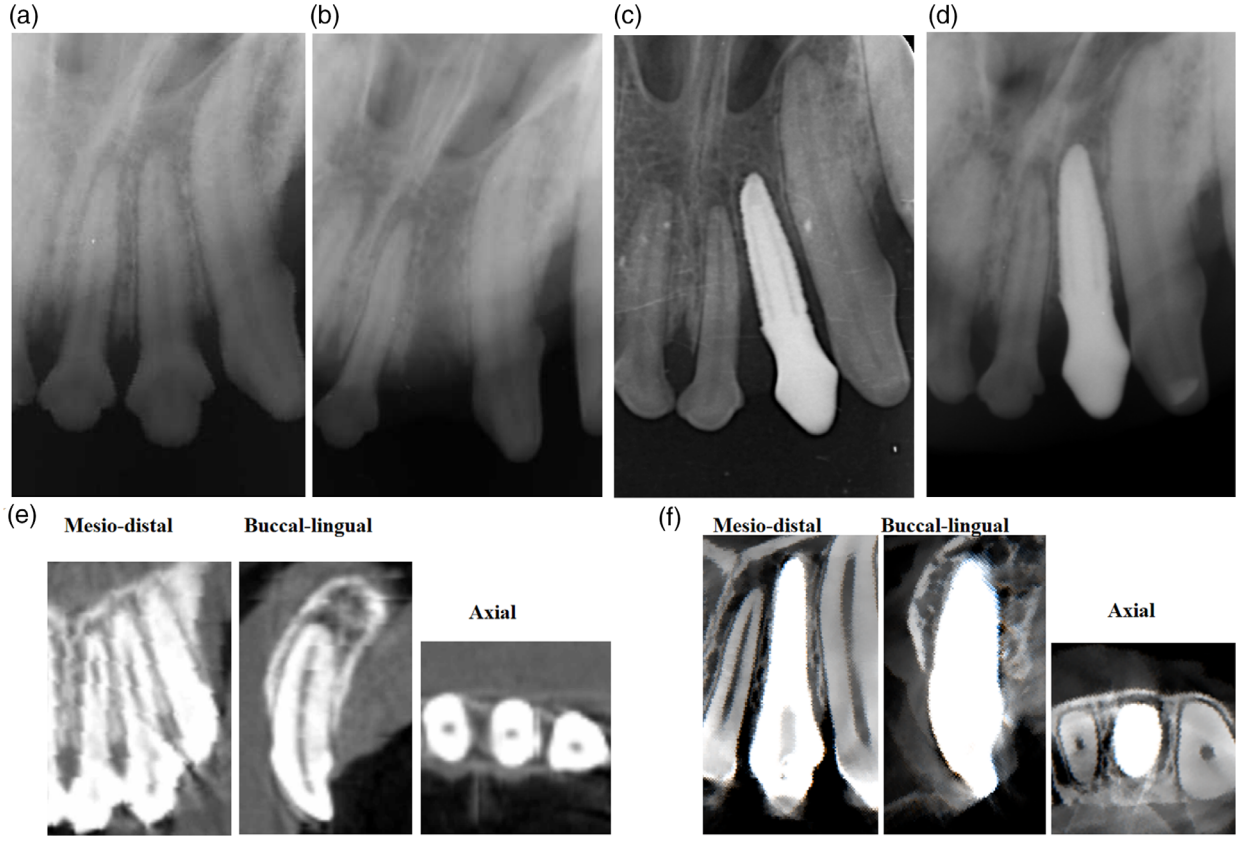

FIGURE 4 (a) Radiographic periapical film of the left upper incisor before surgery. (b) Radiographic periapical film of the extraction socket after minimally invasive extraction. (c) Radiographic periapical film after immediate implantation of Customized Root Implant. (d) Radiographic periapical film 3 months after implantation of Customized Root Implant. (e) Preoperative CT. (f) Micro-CT 3 months after surgery.

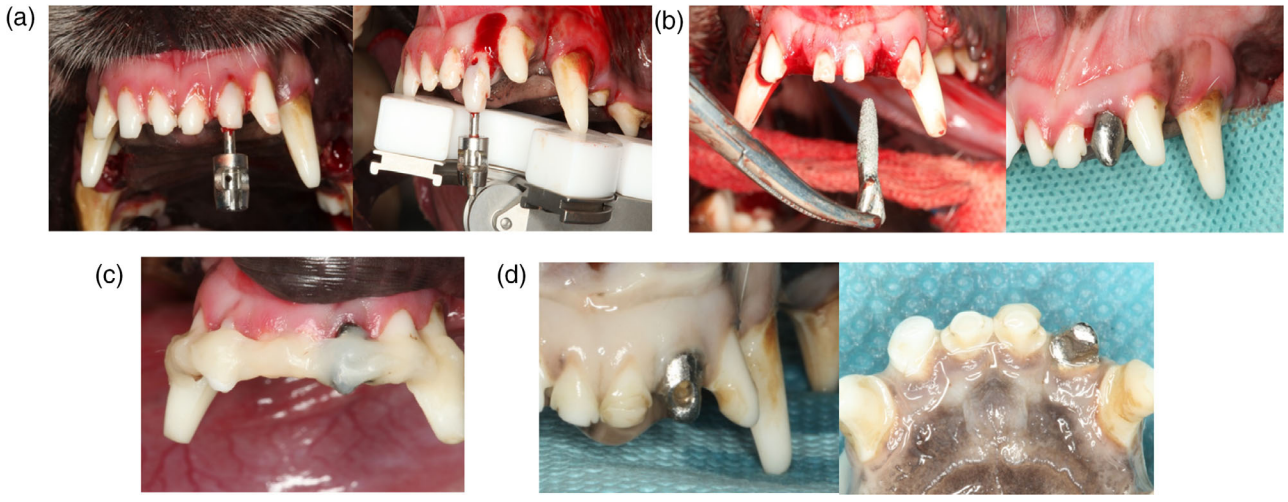

FIGURE 5 (a) Teeth extraction with minimally invasive facilities. (b) Immediate implantation of Customized Root Implant. (c) Strong fiber and flow resin-bonded Customized Root Implant with adjacent teeth. (d) Fixed specimen block after execution.

or bone wall destruction occurred (Fig 4A and B). Strong fiber and flow resin-bonded CRIs with adjacent teeth showed no clinical mobility.

The fiber and flow resin bonded the CRI with adjacent teeth. Therefore, 1 month after surgery, slight redness, and edema of the gums were observed, although the fixing material remained in place and the implant was not loose.

Three months after surgery, there was no redness and swelling of the maxillary anterior teeth gums, and BOP was

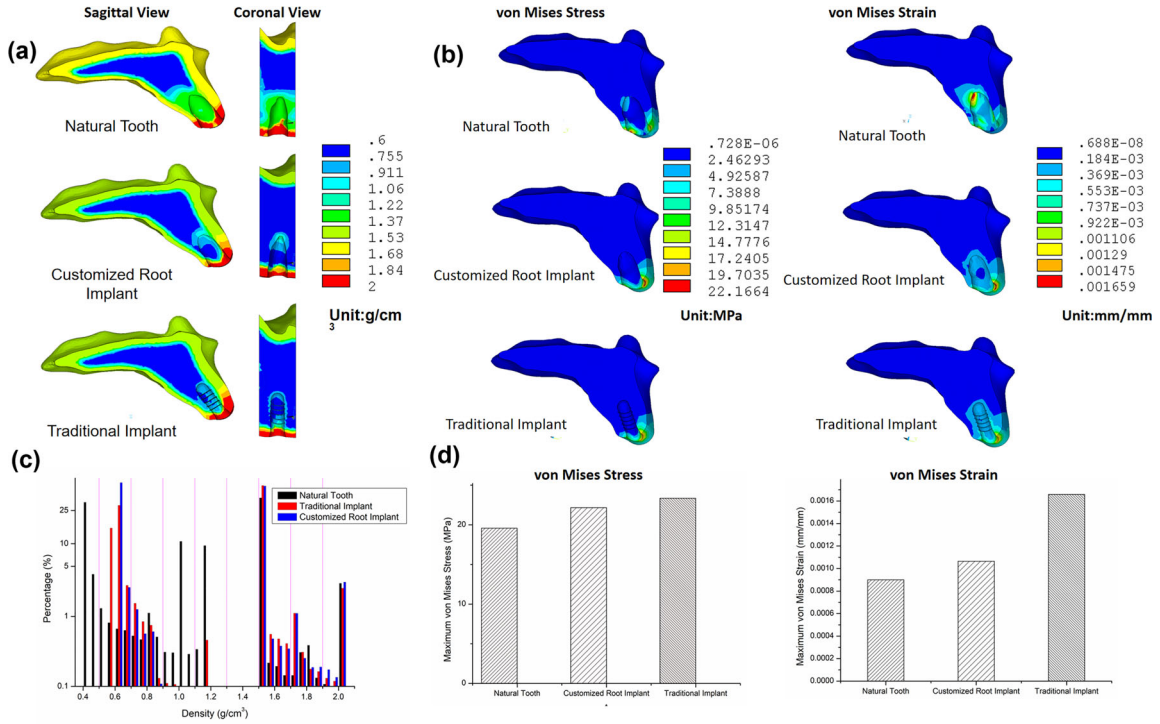

FIGURE 6 (a) Comparison of differences in bone mineral density distribution between the natural tooth model, the CRI model and the traditional implant model due to the bone remodeling mechanism. (b) Comparison of the Mises stress (MPa) and Mises strain (mm/mm) distribution of the three models. (c) Comparison of the bone density values of the three models: natural tooth (black), traditional implant (red), and CRI (blue). This figure showed the percentage of each density value interval in the total density value, which can be used to express the concentration of bone density values in different models. (d) Comparison of the maximum Mises stress (MPa) distribution of the alveolar bone of the three models; Comparison of the maximum Mises strain (mm/mm) distribution of the alveolar bone of the three models.

observed; the PD was 2 to 4 mm, and clinically, no mobility of the implant was detected.

Radiographic inspection

The periapical film after 3 months of implant healing showed no significant low-density transmission around the implant. There was no significant decrease in the height of the adjacent alveolar bone compared to the periapical film immediately after implantation (Fig 4C and D).

Micro-CT analysis

Compared with the preoperative CT (Fig 4E), the micro-CT after 3 months of implant healing showed the trabecular bone in the mesio-distal direction, buccal-lingual direction, and axial direction of the implant. There were no significant changes in height or density (Fig 4F).

Histopathological examination

After hard tissue grinding and toluidine blue staining, the osseointegration interface of the implant after 3 months of healing was abundant and continuous, the new bone trabeculae were dark blue, and the original alveolar bone was light blue. There was no obvious damage or assimilation to the marginal cortical bone of the implant. The new bone area around the cervical region of the CRI was larger than that of the root region, which is consistent with finite element analysis (Fig 7). Microscopic bone tissue grinding images were collected and bone contact rate (bone implant contact, BIC) were measured. And the BIC between the cervical region and the root region were compared (Fig 7C).

DISCUSSION

In this study, quantitative comparison of simulated bone density values showed that, the bone around the natural teeth tended to have a relatively dispersed distribution, while the bone density around the implants was more concentrated. That is to say that the local bone density was higher around both traditional and root implants, compared with natural teeth. The animal experiment result was consistent with finite element model analysis, in other words, the CRI is biomechanically more similar to a conventional cylindrical implant than to a natural tooth, although it closely resembles a natural tooth in appearance.

This finding has great implications for understanding of CRI by clinicians. In clinical application, use of CRI is gradually being considered because of minimally invasive and

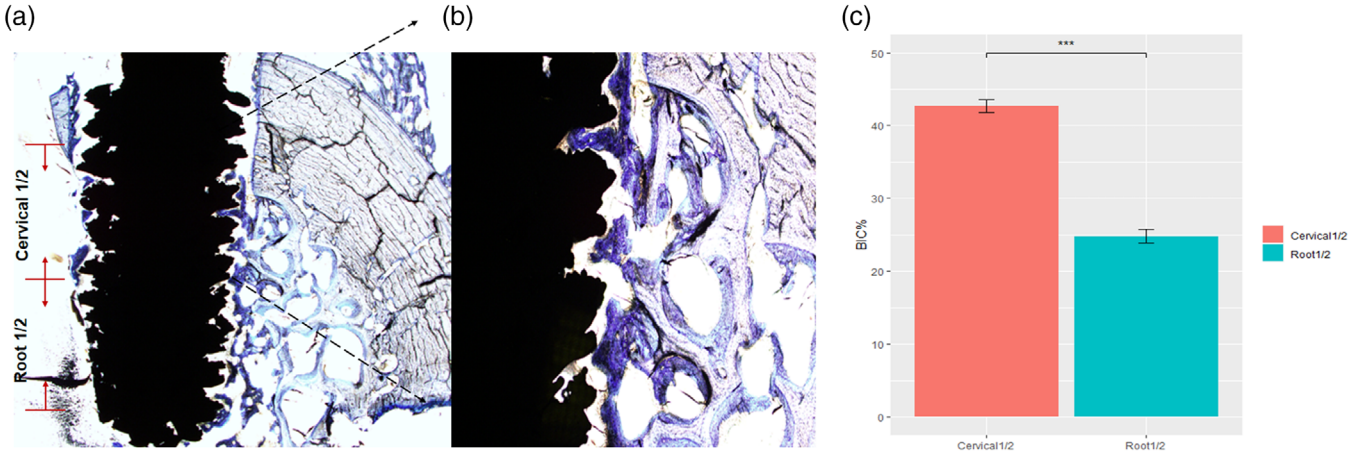

FIGURE 7 Microscopic bone tissue grinding images. (a) 10 times. (b) 40 times. (c) BIC statistics of between the cervical region and the root region.

simple surgery operations, reduced visit time, and to alleviative postoperative reactions. However, the existence of these advantages could not supersede the stress shielding effect in the early application of CRI.[2,3] The results of this study fully demonstrate the current characteristics of CRI, which has a similar appearance to natural teeth but lacks the biomechanical advantages of natural PDL. In fact, for natural teeth, because the periodontium buffers the roots, the alveolar bone density distribution is more uniform, this is more beneficial to the health of the alveolar bone. [22–24] The periodontium can be considered to play a key role in the biomechanical response of natural alveolar bone. Therefore, clinicians should balance the pros and cons, and should carefully select cases to avoid contraindications in order to take full advantages of CRI.

Due to the use of iterative computing technology, the concept of time in the simulation actually represents the number of iterations, and each iteration can be considered to represent a period of time. In the previous studies, Li et al have demonstrated that iterative computation can effectively predict changes in bone mineral density around implants.[22,23,25,26] In this simulation, the calculated bone density converges after about 500 iterations, which can be considered to be equivalent to the completion of bone remodeling of the human skeleton. Sufficient changes in bone mineral density were observed during this simulation period, and the results were consistent with in vivo findings.

In this numerical simulation model, anisotropic material properties are employed to investigate the biomechanical response of CRI. Because dental implantation has always been adhering to the concept of minimal invasive treatment, and CRI requires highly minimally invasive treatment from tooth extraction to implant, with an intact alveolar bone during the surgery process, it can be assumed that the maxillary model has the same degree of anisotropic mechanical properties as natural bone. This method has been successfully applied in many similar dental numerical simulation scenarios. [24,27–29]

According to bone functional adaptation principle,[30] bone tissue is excited according to different mechanical loads to produce corresponding changes in the structure and material properties. Based on the mechanical regulation mechanism (Frost's theory), [31,32] when the mechanical load is below the critical threshold, bone resorption occurs; when the load exceeds the critical threshold, the bone tissue responds positively to bone formation; when the mechanical load is above and below the critical value, bone remodeling is at rest; that is, there is no bone resorption or bone formation; however, when the mechanical load is too large to exceed the normal tolerance range, overload bone resorption occurs. The orthotropic bone remodeling algorithm used in this model was derived from the field of bone tissue research. According to the special features of the maxillofacial bone, the simulation of the maxilla was modified and applied in this study. Since the basic properties of the bone tissue of the maxilla are the same as those of other bone tissues, such transformation has been proven to be feasible and effective by existing research.[33–35]

The biomechanical responses of different models were analyzed and compared herein. The distribution of von Mises stress in the natural tooth model, CRI, and traditional implant model is broadly in the same range (Fig 6B), from 0 to 19.58MPa, 0 to 23.36 MPa, and from 0 to 22.17 MPa, respectively. The high-stress areas of the three models were concentrated in the cervical bone region around the natural tooth and implants, except that in the natural tooth model, there was a small range of stress concentration areas at the root. Figure 6 demonstrates that the maximum von Mises stress of the two implant models is closer, while the maximal von Mises stress of the alveolar bone of the natural tooth model is the smallest. On the other hand, regarding the distribution of von Mises strain, the strain value of the alveolar bone around the natural tooth was small, the maximum value was 0.0970%, and the strain value around the implant was large, around the CRI and the traditional implant were 0.1659% and 0.1065%, respectively. In comparison, the distribution of bone density around the natural tooth was different from that around the implants. The difference between the two implants was small, the strain was mainly

concentrated on the marginal level of the cervical cortical bone region, and the distribution of high strain was limited to a small area (Fig 6B). The bone strain around the natural tooth was more dispersed, from the apical to the cervical region of the root, which is relatively average. The implants significantly altered the original mechanical distribution within the alveolar bone.

In this study, the Beagle's maxilla was used as an in vivo validation test, which corresponds to the human maxillary alveolar bone. Of course, the anatomical structure and physiological function of the occlusal system are greatly different between canines and humans, which is the limitation of this study. Because the growth and development of canines is usually faster than humans, it can be assumed that 3 months post-implantation is sufficient duration for one bone remodeling period.[36–40] After 3 months of the experiment, although no changes in bone mineral density were observed on radiographs, histopathological images showed more new bone in the cervical part of the implant than in the root, which was consistent with the results of simulated analysis.

Another limitation of the study is that only end-point histomorphological data is provided, likewise, the addition of examining the in vivo processes would be valued to understand the adaptation of the bone remodeling. During the experiment, the gingival tissue did not show any erythema or inflammation around the implant, no deep periodontal pocket was probed, and the osseointegration was observed through radiographs and histopathological images. Therefore, it was believed that CRI has good biocompatibility and normal physiological occlusion function in vivo. Although the results of this study fully demonstrate that this model has certain predictability on the CRI and related implants, more histopathological analysis of human subjects is required in future studies to derive more conclusive results.

From a clinical point of view, this new design can improve the practice of clinicians. First of all, the personalized design can make the root shape of the implant exactly match the tooth extraction slot, which is convenient for immediate implantation. Second, because there is no need to prepare the implant hole or the bone graft surgery, the operation is simple and the operation time can be greatly reduced. Third, the porous structure design of CRI is beneficial to maintain the height of alveolar bone wall and avoid unnecessary bone resorption.

CONCLUSION

Despite the limitations of this study, a predictive model was established, and the following conclusions can be drawn.

Although the CRI simulated the shape of the natural teeth root, its biomechanical properties were closer to those of traditional implants because of the absence of periodontium. Through a comparative analysis of the calculated data, it was observed that the bone density, stress, and strain around CRIs were similar to those of traditional implants.

Animal experiments confirmed that CRIs produced by EBM technology can achieve short-term success and achieve the same effect as a traditional implant in a Beagle dog in vivo. Histopathological results strongly demonstrate that CRI can achieve adequate bone integration with its natural anatomical configuration, even without the threaded structure of traditional dental implants.

All in all, the biomechanical calculation and animal evaluation can provide basic theoretical support for further understanding and improvement of CRIs.

ACKNOWLEDGMENTS

This work was supported by Natural Science Foundation of Beijing (grant no. L212063) and the National Key Research and Development Program of China (grant no. 2017YFA0701302, PKUSS20200113), the National Natural Science Foundation of China (grant no. 11872135, 12072055, U20A20390).

CONFLICT OF INTEREST

The authors do not have any conflicts of interest in regards to the current study.

ORCID

Xinyue Zhang ME https://orcid.org/0000-0001-6398-8050
Chao Wang PhD https://orcid.org/0000-0001-7792-9887

REFERENCES

1. Lin C, Hu H, Zhu J, Wu Y, Rong Q, Tang Z. Influence of sagittal root positions on the stress distribution around custom-made root-analogue implants: a three-dimensional finite element analysis. BMC Oral Health. 2021;21:443. doi:10.1186/s12903-021-01809-4
2. Böse MWH, Hildebrand D, Beuer F, Wesemann C, Schwerdtner P, Pieralli S, et al. Clinical outcomes of root-analogue implants restored with single crowns or fixed dental prostheses: a retrospective case series. J Clin Med. 2020;9:2346. doi:10.3390/jcm9082346
3. Dantas T, Madeira S, Gasik M, Vaz P, Silva F. Customized root-analogue implants: a review on outcomes from clinical trials and case reports. Materials (Basel). 2021;14. doi:10.3390/ma14092296
4. Ramakrishnaiah R, Al Kheraif AA, Mohammad A, Divakar DD, Kotha SB, Celur SL. et al. Preliminary fabrication and characterization of electron beam melted Ti-6Al-4V customized dental implant. Saudi J Biol Sci. 2017;24:787-796
5. Figliuzzi M, Giudice A, Rengo C, Fortunato L. A direct metal laser sintering (DMLS) root analogue implant placed in the anterior maxilla. Case report. Ann Ital Chir. 2019;8: S2239253X19030044
6. Song K, Wang Z, Lan J, Ma S. Porous structure design and mechanical behavior analysis based on TPMS for customized root analogue implant. J Mech Behav Biomed Mater. 2021;115:104222. doi:10.1186/s12903-021-01809-4
7. Mangano FG, De Franco M, Caprioglio A, Macchi A, Piattelli A, Mangano C. Immediate, non-submerged, root-analogue direct laser metal sintering (DLMS) implants: a 1-year prospective study on 15 patients. Lasers Med Sci. 2014;29:1321-1328
8. Liu T, Chen Y, Apicella A, Mu Z, Yu T, Huang Y, et al. Effect of porous microstructures on the biomechanical characteristics of a root analogue implant: an animal study and a finite element analysis. ACS Biomater Sci Eng. 2020;6:6356-6367
9. Westover B. Three-dimensional custom-root replicate tooth dental implants. Oral Maxillofac Surg Clin North Am. 2019;31:489-496

10. Han J, Sun Y, Wang C. Effect of integration patterns around implant neck on stress distribution in peri-implant bone: a finite element analysis. J Prosthodont. 2017;26:549-558
11. Wang L, Wu Y, Perez KC, Hyman S, Brunski JB, Tulu U, et al. Effects of condensation on peri-implant bone density and remodeling. J Dent Res. 2017;96:413-420
12. I-Chiang C, Shyh-Yuan L, Ming-Chang W, Sun CW, Jiang CP. Finite element modelling of implant designs and cortical bone thickness on stress distribution in maxillary type IV bone. Comput Methods Biomech Biomed Eng. 2014;17:516-526
13. Field C, Li Q, Li W, Thompson M, Swain M. A comparative mechanical and bone remodelling study of all-ceramic posterior inlay and onlay fixed partial dentures. J Dent. 2012;40:48-56
14. Lin CL, Lin YH, Chang SH. Multi-factorial analysis of variables influencing the bone loss of an implant placed in the maxilla: prediction using FEA and SED bone remodeling algorithm. J Biomech. 2010;43:644-651
15. Chou HY, Jagodnik JJ, Müftü S. Predictions of bone remodeling around dental implant systems. J Biomech. 2008;41:1365-1373
16. Ashman RB, Van Buskirk WC. The elastic properties of a human mandible. Adv Dent Res. 1987;1:64-67
17. Lowet G, Van Audekercke R, Van der Perre G, Geusens P, Dequeker J, Lammens J. The relation between resonant frequencies and torsional stiffness of long bones in vitro. Validation of a simple beam model. J Biomech. 1993;26:689-696
18. Rho JY, Hobatho MC, Ashman RB. Relations of mechanical properties to density and CT numbers in human bone. Med Eng Phys. 1995;17:347-355
19. O'Mahony AM, Williams JL, Katz JO, Spencer P. Anisotropic elastic properties of cancellous bone from a human edentulous mandible. Clin Oral Implants Res. 2000;11:415-421
20. Li J, Li H, Shi L, Fok AS, Ucer C, Devlin H, et al. A mathematical model for simulating the bone remodeling process under mechanical stimulus. Dent Mater. 2007;23:1073-1078
21. Mellal A, Wiskott HW, Botsis J, Scherrer SS, Belser UC. Stimulating effect of implant loading on surrounding bone. Comparison of three numerical models and validation by in vivo data. Clin Oral Implants Res. 2004;15:239-248
22. Lin D, Li Q, Li W, Duckmanton N, Swain M. Mandibular bone remodeling induced by dental implant. J Biomech. 2010;43: 287-293
23. Lin D, Li Q, Li W, et al: Design optimization of functionally graded dental implant for bone remodeling. Compos B Eng. 2009;40:668-675
24. Wang C, Wang L, Liu X, Fan Y. Numerical simulation of the remodelling process of trabecular architecture around dental implants. Comput Methods Biomech Biomed Eng. 2014;17:286-295
25. Li W, Lin D, Rungsiyakull C, et al. Finite element based bone remodeling and resonance frequency analysis for osseointegration assessment of dental implants. Finite Elem Anal Des. 2011;47:898-905
26. Field C, Li Q, Li W, Swain M. Prediction of mandibular bone remodeling induced by fixed partial dentures. J Biomech. 2010;43:1771-1779
27. Wang C, Li Q, McClean C, Fan Y. Numerical simulation of dental bone remodeling induced by implant-supported fixed partial denture with or without cantilever extension. Int J Numer Meth Biomed Eng. 2013;29:1134-1147
28. Wang C, Fu G, Deng F. Difference of natural teeth and implant-supported restoration: a comparison of bone remodeling simulations. J Dent Sci. 2015;10:190-200
29. Wang C, Zhang W, Ajmera DH, Zhang Y, Fan Y, Ji P. Simulated bone remodeling around tilted dental implants in the anterior maxilla. Biomech Model Mechanobiol. 2016;15:701-712
30. Frost HM. Bone's mechanostat: a 2003 update. Anat Rec A. 2003;275:1081-1101
31. Frost HM. Skeletal structural adaptations to mechanical usage (SATMU): 2. Redefining Wolff's law: the remodeling problem. Anat Rec. 1990;226:414-422
32. Frost HM. Skeletal structural adaptations to mechanical usage (SATMU): 1. Redefining Wolff's law: the bone modeling problem. Anat Rec. 1990;226:403-413
33. Papadopoulou K, Hasan I, Keilig L, Reimann S, Eliades T, Jäger A, et al. Biomechanical time dependency of the periodontal ligament: a combined experimental and numerical approach. Eur J Orthod. 2013;35:811-888
34. Aversa R, Apicella D, Perillo L, Sorrentino R, Zarone F, Ferrari M, et al. Non-linear elastic three-dimensional finite element analysis on the effect of endocrown material rigidity on alveolar bone remodeling process. Dent Mater. 2009;25:678-690
35. Lin D, Li Q, Li W, Swain M. Dental implant induced bone remodeling and associated algorithms. J Mech Behav Biomed Mater. 2009;2:410-432
36. Roberts WE, Roberts JA, Epker BN, Burr DB, Jr J. Remodeling of mineralized tissues, part I: the frost legacy. Semin Orthod. 2006;12: 216-237
37. Roberts WE, Epker BN, Burr DB, et al. Remodeling of mineralized tissues, part II: control and pathophysiology. Semin Orthod. 2006;12: 238-253
38. Roberts WE, Huja S, Roberts JA. Bone modeling: biomechanics, molecular mechanisms, and clinical perspectives. Semin Orthod. 2004;10: 123-161
39. Caroprese M, Lang NP, Rossi F, Ricci S, Favero R, Botticelli D. Morphometric evaluation of the early stages of healing at cortical and marrow compartments at titanium implants: an experimental study in the dog. Clin Oral Implants Res. 2016;28:1030-1037
40. Kimmel DB, Jee W. A quantitative histologic study of bone turnover in young adult beagles. Anatoml Record. 2010;203:31-45

How to cite this article: Li Q, Zhang Q, Wang C, Hu H, Tang Z, Fan Y. Biomechanical evaluation of customized root implants in alveolar bone: A comparative study with traditional implants and natural teeth. J Prosthodont. 2022;1–11. https://doi.org/10.1111/jopr.13590